Cycloidal Propulsion of Submersibles

MICHAEL A. RICKARDS*
Weber Aircraft, Burbank, Calif.

The concepts of 1) true advance ratio and 2) normalized blade pitch ratio are introduced and discussed in terms of pertinent cycloidal propulsion criteria. The equations of motion pertaining to the blade dynamics of cycloidal propulsion are presented. Numerical results from a computer study are discussed. Kramer's effect and hydrodynamic hysteresis are included in the determination of propeller torque and force coefficients.

Introduction

THE path followed by a point on a wheel rolling on a flat surface without slipping, traces a true "cycloidal" curve. The blade of a cycloidal propeller advancing in space traces, in fact, a true cycloidal curve; hence the name "cycloidal propeller." This unique propulsor was first introduced by F. K. Kirsten, at the University of Washington, when he filed for a U. S. patent application, in 1922. The first comprehensive paper on cycloidal propulsion appeared in 1928 when Kirsten introduced "A New Type of Propeller" to the Society of Automotive Engineers.[1]

The first outstanding trait of this propulsor is the relative ease with which it accommodates a full 360° thrust orientation at stationary vehicle (hovering) conditions as well as at high speeds. Secondly, at cruising conditions, the propeller blades do not stall and consequently are not prone to cavitation and excess noise due to turbulence. The third conspicuous distinction, autostability, was first demonstrated by L. W. Seely[2] in 1963 by means of a simple mathematical model. Autostability causes an induced change in the resultant thrust due to a perturbation from equilibrium that tends to neutralize the perturbation. This phenomenon has been observed for instance in connection with speedboats and barges cycloidally propelled through a cross current. It is little wonder, therefore, that various forms of cycloidal propulsors[3,4] for surface vehicles have been developed by the Marine industry. A natural extension is the application of cycloidal propulsion on submersibles.

Mechanics of Cycloidal Propulsion

Consider points a, b, c, and d on the outside surface of a "train wheel" rolling without slipping along a straight track as shown in Fig. 1. As the wheel rolls, these points correspondingly trace paths A, B, C, and D in space. The path A generated by the center of the wheel is, of course, a straight line parallel to the rolling plane (rail). It is located a distance R_0 above the rolling plane. The radius R_0 represents the rolling radius at zero slip. The paths B, C, and D all trace cycloidal paths, correspondingly classified as "curate," "ordinary," and "prolate" cycloids. A parameter known as the pitch ratio p classifies the cycloidal curve in question

$$p \equiv \pi R_0/R \tag{1}$$

If the pitch ratio is zero, less than π, equal to π, or greater than π, the corresponding curves generated are a circle, a prolate cycloid, an ordinary cycloid, and a curtate cycloid. The pitch ratio, as defined in Eq. (1), represents the distance advanced per revolution in terms of the generating diameter. Assume in Fig. 1 that the path A is generated at a speed V, known as the "speed of advance." Assume further that the wheel is now slipping on the slip-roll surface located a distance R_S from the center of the wheel. The speed of advance is related to the angular rotation of the wheel, ω, by the "true advance ratio" Λ, introduced as follows:

$$\Lambda \equiv V/\omega R_S = R_0/R_S \tag{2}$$

From the first equality of Eq. 2, the true advance ratio is seen to be the ratio of the actual velocity of advance of the slipping "train wheel" to that at "would-be" zero slip. A distinction between the slip-roll radius R_S and the equivalent no-slip rolling radius R_0 must be made. The cycloidal curve generated by a slip-roll surface is a "pseudocycloid" that is identifiable through superposition to an equivalent "true" cycloid of zero-slip rolling radius R_0, that is smaller than R_S. The actual speed of advance V, is therefore identically, ωR_0, which justifies the second equality given in Eq. (2). Henry[4] defines the advance ratio λ as R_0/R which in reality is an apparent advance ratio. Equation (2) is more conducive to physical interpretation and representative of the reciprocal nature between the concept of "advance ratio" and "slip-ratio." The slip-ratio σ is defined as the normalized ratio of the difference between the would-be speed of advance at zero slip and the actual speed of advance

$$\sigma \equiv \omega(R_S - R_0)/\omega R_S = 1 - \Lambda \tag{3}$$

A zero-slip condition, $\sigma = 0$, is therefore synonymous to an advance ratio of unity and vice versa. In Fig. 1, let a propeller blade assume a distance R from the center of the wheel. Furthermore, assume that the blade chord has a built-in capability of angular orientation with respect to the generating radius R. The geometry pertaining to this propeller blade

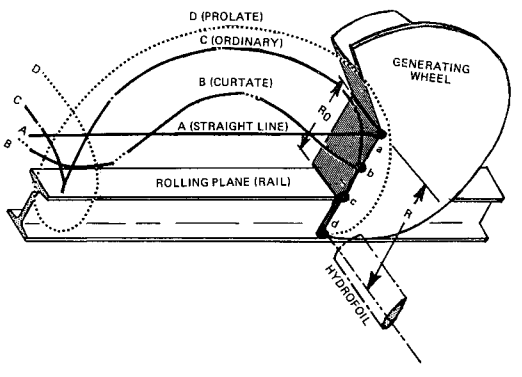

Fig. 1 Trainwhell analogy. Cycloidal curves are generated by the whell rolling at zero slip.

Presented as Paper 69-391 at the AIAA 2nd Advanced Marine Vehicles and Propulsion Meeting, Seattle, Wash., May 21–23, 1969; submitted April 16, 1969; revision received October 6, 1969.

* Chief Scientist, Advance Concept Research Department. Associate Fellow AIAA.

in cycloidal motion is shown in Fig. 2. Let the D (drag) axis be directed opposite to the path of advance and the L (lift) axis be perpendicular to both D and the axis of rotation ω ($L \times \omega$ is a vector in the direction of D). All angles and moments in this study are taken as positive in a counterclockwise ($D \times L$ vector) direction. The blade is shown instantaneously at point P. The orbital radius R is angularly displaced from the D axis by the angle of orbit θ. The blade angle β is the angle subtended from the tangent line of the blade path at point P (perpendicular to R) to the blade chordline. A line perpendicular to the blade chordline intersects the Y axis at the point S known as the "instantaneous steering center." The point S defines the slip-roll surface of the train wheel model analogy introduced in Eq. (2). It is consequently located at a radial distance R_s from the origin and is displaced angularly from the L axis by the displacement angle δ. The normalized blade pitch ratio is introduced in Eq. (4)

$$\eta \equiv R_S/R \tag{4}$$

The normalized blade pitch ratio does not change with slip ratio, whereas p does since it defines the instantaneous cycloidal path. The parameter η therefore properly describes the given cycloidal propeller design. The π-pitched (Kirsten) propeller often seen in the literature really implies $\eta = 1$ and not $p = \pi$. The tangential velocity of the blade ωR adds vectorially to the velocity of advance V to yield the resultant blade velocity W. The angle subtended by W and the orbit tangent line at P is the blade path angle γ. The angle of attack α_0 is the angle between the chordline and the resultant relative blade velocity W. The blade angle may be described in general as

$$\beta \equiv \beta(\theta,\eta,\delta) \tag{5}$$

From Fig. 2, the instantaneous blade angle can be shown to be

$$\beta = \tan^{-1}\{\eta \cos(\theta - \delta)/[1 + \eta \sin(\theta - \delta)]\} \tag{6}$$

Define the relative orbit angle ξ as follows:

$$\xi = \theta + \pi/2 - \delta \tag{7}$$

In terms of the relative orbit angle, Eq. (6) reduces to

$$\beta = \tan^{-1}[\eta \sin\xi/(1 - \eta \cos\xi)] \tag{8}$$

From Fig. 2,

$$\alpha_0 \equiv \beta - \gamma \tag{9}$$

Also, from the velocity-vector triangle shown in Fig. 2,

$$\gamma = \tan^{-1}\{\cos\theta/[(\omega R/V) + \sin\theta]\} \tag{10}$$

The parameter $\omega R/V$, from Eqs. (2) and (4) may be shown to be related to the blade pitch ratio η and the true advance ratio Λ

$$\omega R/V = (\omega R_S/V)(R/R_S) = 1/\eta\Lambda = 1/\lambda \tag{11}$$

The parameter $\lambda = V/\omega R$ introduced in Eq. (11) is the apparent advance ratio which is identically the ratio R_0/R. Combining Eqs. (6, 9, 10, and 11), the orbital angle of attack is

$$\alpha_0 = \tan^{-1}\left[\frac{\eta \cos(\theta - \delta)}{1 + \eta \sin(\theta + \delta)}\right] - \tan^{-1}\left[\frac{\lambda \cos\theta}{1 + \lambda \sin\theta}\right] \tag{12}$$

Reverting back to Fig. 2, construct the line $S_0 - P$ such that it is perpendicular to the resultant blade velocity W and such that it intersects the L axis at S_0. The radius R_0 represents the "equivalent" rolling radius at zero slip. This fact was very well demonstrated by Henry[4] by comparing the velocity vector triangle with the similar triangle OPS_0. The location of S_0 remains unaltered as long as $V/\omega R$ is constant

$$R_0/R = V/\omega R = \lambda \tag{13}$$

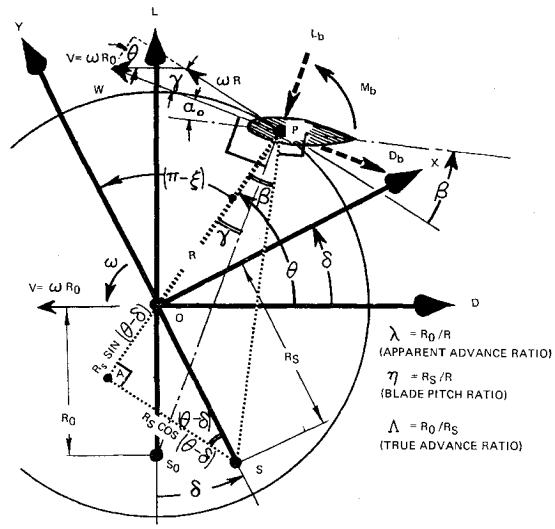

Fig. 2 The mechanics of cycloidal propulsion.

The "apparent advance ratio" λ relates the speed of advance to the blade orbital speed regardless of the type of cycloid generated. The true advance ratio is obtained as follows:

$$R_0/R_S = (R_0/R)(R/R_S) = V/\omega R_S = \Lambda \tag{14}$$

The ratio R_0/R_s is therefore, in fact, the true advance ratio Λ. The true advance ratio Λ is related to p and η as follows:

$$\Lambda = p/\pi\eta \tag{15}$$

Forces and Moments

The resultant (average) of all forces and moments experienced by the blade per orbit may be resolved into a force vector and a moment about the orbital axis of rotation expressed in dimensionless coefficients. The maximum relative velocity experienced by the orbiting blade appears to be the reasonable velocity parameter to employ for the normalization of forces and moments. The force and moment coefficients defined in this form remain finite at $V = 0$ and exhibit a handy basis of comparison for different η at finite true advance ratios. The resultant cycloidal force and moment coefficients originating from the center of orbit follow:

$$C_R \equiv \frac{F_R}{1/2\rho(\omega R + V)^2(\pi R^2)} = \frac{2F_R}{\pi\rho\omega^2R^4(1 + V/\omega R)^2} \tag{16}$$

$$C_{m_0} \equiv \frac{M_0}{1/2\rho(\omega R + V)^2(\pi R^2)R} = \frac{2M_0}{\pi\rho\omega^2R^5(1 + V/\omega R)^2} \tag{17}$$

In Eqs. (16) and (17), as in Eq. (12), it becomes noticeable that the apparent advance ratio, $\lambda = V/\omega R$, plays a significant role. The resultant force can be further subdivided into lift and drag components

$$C_L = 2L/\pi\rho\omega^2R^4(1 + \lambda)^2 \tag{18}$$

$$C_D = 2D/\pi\rho\omega^2R^4(1 + \lambda)^2 \tag{19}$$

The lift L, drag D, and pitching moment Mo, relative to the blade orbit geometry given in Fig. 2, is shown in normalized form in Fig. 3. The subsequent relations follow readily from Fig. 3:

$$\sin\gamma = \lambda \cos\theta/(1 + 2\lambda \sin\theta + \lambda^2)^{1/2} \tag{20}$$

$$\cos\gamma = (1 + \lambda \sin\theta)/(1 + 2\lambda \sin\theta + \lambda^2)^{1/2} \tag{21}$$

$$\sin(\theta - \gamma) = (\lambda + \sin\theta)/(1 + 2\lambda \sin\theta + \lambda^2)^{1/2} \tag{22}$$

$$\cos(\theta + \gamma) = \cos\theta/(1 + 2\lambda \sin\theta + \lambda^2)^{1/2} \tag{23}$$

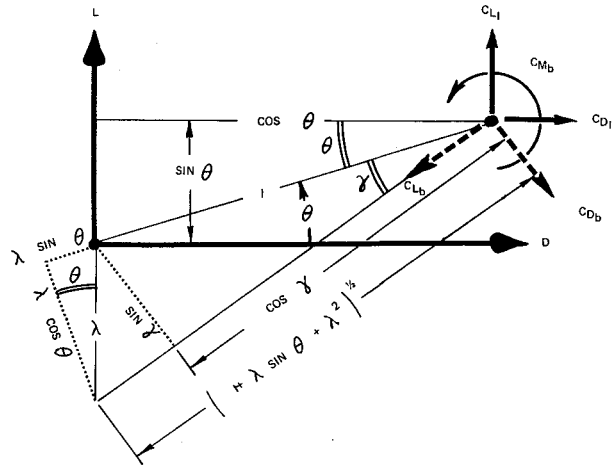

Fig. 3 Normalized blade orbit geometry.

The instantaneous hydrodynamic coefficients, based on the blade area S_b, blade chord C, and total relative velocity W are denoted: C_{Lb} for the lift coefficient, C_{Db} for the drag coefficient, and C_{mb} for the pitching moment coefficient. Their instantaneous contribution to the cycloidal lift, drag, and pitching moment (L-D axis in Fig. 3) is

$$C_{Li} = -C_{Lb}\sin(\theta + \gamma) - C_{Db}\cos(\theta + \gamma) \quad (24)$$

$$C_{Di} = C_D \sin(\theta + \gamma) - C_{Lb}\cos(\theta + \gamma) \quad (25)$$

$$C_{mi} = C_{mb} - (R/C)(C_{Db}\cos\gamma + C_{Lb}\sin\gamma) \quad (26)$$

Substituting the relations given in Eqs. (20–23) into Eqs. (24–26),

$$C_{Li} = \frac{-C_{Lb}(\lambda + \sin\theta) - C_{Db}\cos\theta}{(1 + 2\lambda\sin\theta + \lambda^2)^{1/2}} \quad (27)$$

$$C_{Di} = \frac{-C_{Lb}\cos\theta + C_{Db}(\lambda + \sin\theta)}{(1 + 2\lambda\sin\theta + \lambda^2)^{1/2}} \quad (28)$$

$$C_{mi} = C_{mb} + \left(\frac{R}{C}\right)\frac{[C_{Lb}\lambda\cos\theta + C_{Db}(1 + \lambda\sin\theta)]}{(1 + 2\lambda\sin\theta + \lambda^2)^{1/2}} \quad (29)$$

Notice from Eqs. (27) and (28) that

$$C_{Li}^2 + C_{Di}^2 = C_{Lb}^2 + C_{Db}^2 \quad (30)$$

Let the blade area ratio be

$$B = \Sigma S_b/\pi R^2 \quad (31)$$

The resultant lift, drag, and pitching moment coefficients are found by averaging (per orbit revolution) the forces and

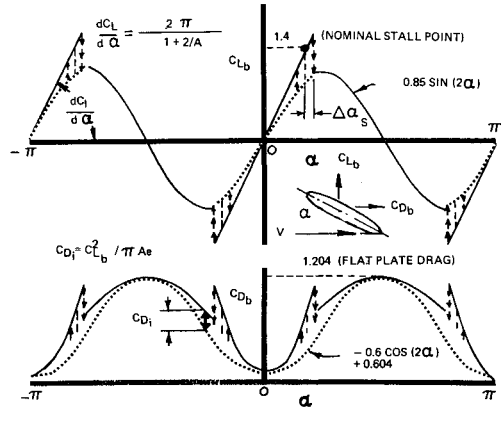

Fig. 4 Lift and drag coefficient model for a fully symmetrical hydrofoil of 0.09 thickness ratio.

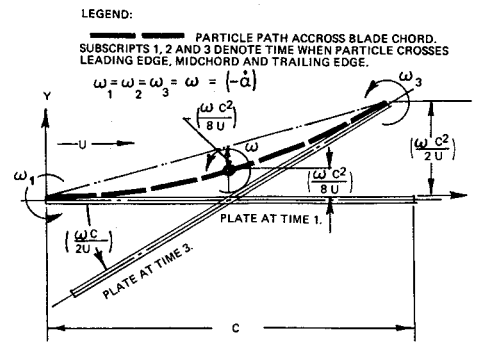

Fig. 5 Effective camber due to blade rotation.

moments given by Eqs. (27–29). These must be accommodated by the blade area ratio B, and also by the parameter $W/(\omega R + V)^2 = (1 + \lambda^2)/(1 + \lambda)^2$. The former parameter accounts for a change in reference areas from the blade area into the blade orbit area πR^2. The latter parameter redefines the reference velocity from the actual velocity experienced by the blade, W, into the maximum scalar speed $(V + \omega R)$. The cycloidal force and moment coefficients in the light of definitions, Eqs. (16–19) are

$$C_R = \frac{B(1 + \lambda^2)}{2\pi(1 + \lambda)^2} \times \left\{\left[\int_0^{2\pi} \frac{-C_{cb}(\lambda + \sin\theta) - C_{Db}\cos\theta)}{(1 + 2\lambda\sin\theta + \lambda^2)^{1/2}}\, d\theta\right]^2 + \left[\int_0^{2\pi} \frac{-C_{cb}\cos\theta + C_{Db}(\lambda + \sin\theta)}{(1 + 2\lambda\sin\theta + \lambda^2)^{1/2}}\right]^2\right\}^{1/2} \quad (32)$$

$$C_{m_0} = \frac{B(1 + \lambda^2)}{(1 + \lambda)^2}\left[C_{mb}\frac{C}{R} + \frac{1}{2\pi}\int_0^{2\pi} \frac{C_{Lb}\lambda\cos\theta + C_{Db}(1 + \lambda\sin\theta}{(1 + 2\lambda\sin\theta + \lambda^2)^{1/2}}\, d\theta\right] \quad (33)$$

$$C_L = \frac{B(1 + \lambda^2)}{2\pi(1 + \lambda)^2}\int_0^{2\pi} \frac{-C_{Lb}(\lambda + \sin\theta) - C_{Db}\cos\theta}{(1 + 2\lambda\sin\theta + \lambda^2)^{1/2}}\, d\theta \quad (34)$$

$$C_D = \frac{B(1 + \lambda^2)}{2\pi(1 + \lambda)^2}\int_0^{2\pi} \frac{-C_{Lb}\cos\theta + C_{Db}(\lambda + \sin\theta)}{(1 + 2\lambda\sin\theta + \lambda^2)^{1/2}}\, d\theta \quad (35)$$

Blade Force Coefficients

Equations (33–35) fully describe the cycloidal propeller forces and moments as a function of the apparent advance ratio λ and the propeller blade design. The blade coefficients are a function of the instantaneous angle of attack α_0, and rate of change of angle of attack $\dot{\alpha}_0$ (Kramer's effect) as well as the physical airfoil characteristics of the blade itself. Figure 4 presents a proposed idealized dependence of lift and drag coefficients on angle of attack throughout a 360° range. The slope of the linear portion of the lift curve is a function of the effective blade aspect ratio. This slope is[5]

$$dC_L/d\alpha = a_0/(1 + a_0/\pi A) \quad (36)$$

where a_0 = two dimensional lift curve slope of the airfoil in question, and A = effective aspect ratio of the blade.

The linear portion of the lift curve suffers an abrupt degradation at the stall angle α_s. The stall angle depends largely on whether the blade progresses from the unstalled to the stalled region or vice versa[6] as depicted by the arrows in Fig. 4. This peculiar neighborhood of stall, $\Delta\alpha_s$, is a consequence of hydrodynamic (or aerodynamic) "hysteresis." The magnitude of $\Delta\alpha_s$, depends largely on the rate of change of angle of attack, $\dot{\alpha}_s$. For $\dot{\alpha}_s$ approaching zero, the angle of

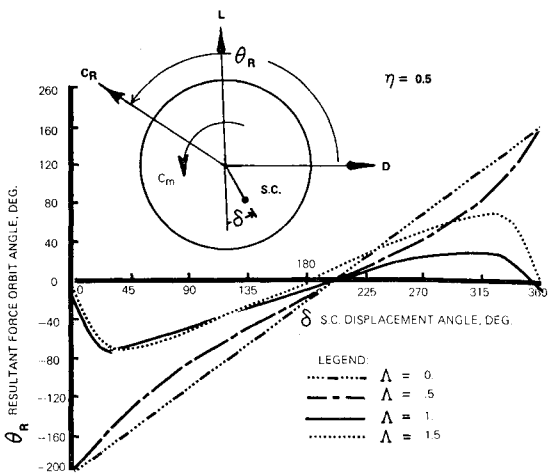

Fig. 6 Resultant force orbit angle vs steering center displacement angle for a pitch ratio of 0.5 and true advance ratios from 0 to 1.5.

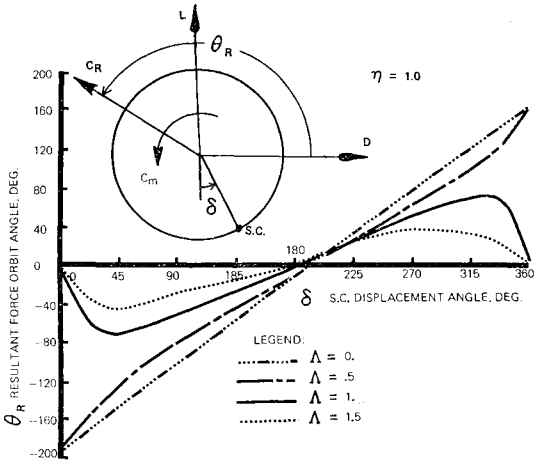

Fig. 7 Resultant force orbit angle vs steering center displacement angle for a pitch ratio of 1.0 and true advance ratios from 0 to 1.5.

hysteresis[6] is approximately 2.5°. At larger values of $\dot{\alpha}_s$ the approximate equation is proposed

$$\Delta\alpha_S \approx \dot{\alpha}_s C \cos\alpha/2W| = \left|\frac{\dot{\alpha}_c C \cos\alpha_s/2\omega R}{(1+\lambda^2)^{1/2}}\right| \tag{37}$$

Equation (37) physically represents the angle by which the blade rotates relative to the airstream during the time an air particle travels a distance from the leading edge to the blade half-chord. The half-chord point was chosen as the downstream limit since a major portion of the hydrodynamic pressure is generated ahead of the half-chord of the propeller blade. The angle $\Delta\alpha_s$ is further degraded by the cosα since at $\alpha = 90°$, hysteresis is nonexistent. Furthermore, there must be an upper limit imposed to the maximum allowable change in blade stall angle or else the point of stall would endlessly increase with $\dot{\alpha}_s$, which is an absurdity. A reasonable limit to impose is the angle corresponding to the maximum achievable lift coefficient of a fully flapped airfoil. For airfoil sections of average thickness, a value of $C_{Lb} = 2.2$ is a reasonable maximum to employ and has been utilized in the computer study. The effect of camber in an airfoil is to shift the lift curve along the angle of attack axis. In cycloidal propellers, due to the cyclic response of the rate of change of angle of attack, even a symmetrical airfoil exhibits an effective camber that continually changes during the orbit. This effect is known as Kramer's effect.

Kramer's Effect

Since Kramer's effect manifests itself in an effective camber at an (induced) angle of attack, a very thin flat-plate model suffices to predict its hydrodynamic character. Consider a thin flat plate of chord length C at zero angle of attack but rotating relative to the airstream at a rate $\omega = (-\dot{\alpha})$. From Fig. 5, a particle of fluid moving across the blade chord and adjacent to it is accelerated (in the Y direction) such that at all times the resultant particle velocity follows the instantaneous blade direction. Let U be the velocity component parallel to the flat-plate at time $t = 0$. Since the particle path slope is equal to the instantaneous plate slope at $x = Ut$,

$$dy/dx = \omega t = \omega x/U \tag{38}$$

At the trailing edge ($x = C$)

$$(dy/dx)_c = \omega C/U \tag{39}$$

Integrating Eq. (38) from zero to x

$$y = \omega x^2/2U \tag{40}$$

Were the blade rotating about the leading edge, the presence of coriolis acceleration would have provided a value of y twice that shown in Eq. (40). Equation (40) corresponds to a chordwise moving center of rotation that follows the particle motion along the blade chord and only the purely rotational contribution remains significant. Since $\omega = -\dot{\alpha}$,

$$Y_C = (-\dot{\alpha})C^2/2U \tag{41}$$

$$dY_C/dt = (-\dot{\alpha})C/U \tag{42}$$

The induced angle of attack of the cambered airfoil is

$$\Delta\alpha_C = Y_c/C = (-\dot{\alpha})C/2U \tag{43}$$

For small values of $(\dot{\alpha}C/U)$, the maximum camber ordinate is approximately

$$(\Delta Y)_{c/2} \approx Y_c/2 - (-\dot{\alpha})(C/2)^2/2U = (-\dot{\alpha})C/8U \tag{44}$$

From wind-tunnel data,[7] the effective lift coefficient due to this camber (at zero angle of attack) can be empirically approximated as

$$\Delta C_L \approx (\Delta Y)_{c/2}/0.05515 = 2.27\dot{\alpha}C/U \tag{45}$$

The total contribution of lift coefficient due to Kramer's effect is accordingly

$$\Delta C_{Lb} = (\dot{\alpha}C/2U)(dC_L/d\alpha + 4.54) \tag{46}$$

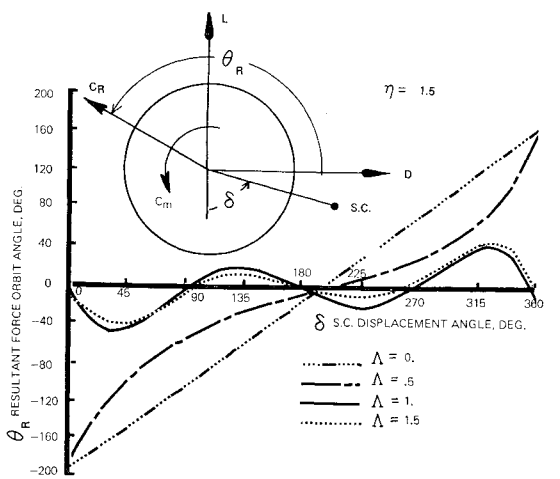

Fig. 8 Resultant force orbit angle vs steering center displacement angle for a pitch ratio of 1.5 and true advance ratios from 0 to 1.5.

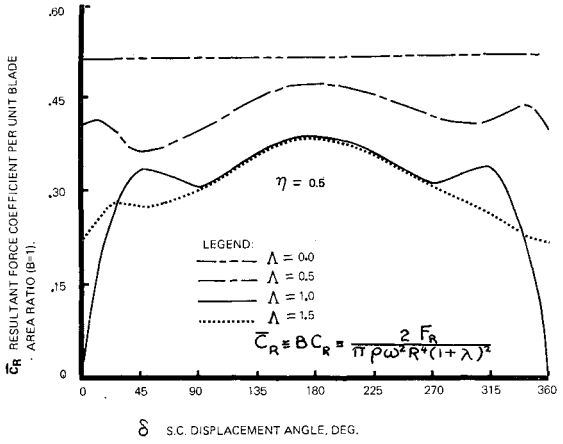

Fig. 9 Resultant force coefficient per unit blade area ratio vs the steering center displacement angle for a pitch ratio of 0.5 and true advance ratios from 0 to 1.5.

The first term arises from the induced angle of attack [Eq. (43)] of the generated cambered surface and the second term is the contribution of camber alone [Eq. (45)]. The pitching moment about the quarter-chord generated by this camber is

$$\Delta C_{mb} = (dC_L/d\alpha)(\dot{\alpha}C/8U) \approx 0.568\dot{\alpha}C/U \qquad (47)$$

The velocity U is equal to $\omega R(1 + \lambda^2)^{1/2} \cos\alpha$, consequently

$$\Delta C_{Lb} = \left[\frac{a_0}{1 + a_0/\pi A} + 4.54\right] \frac{(\dot{\alpha}C/\omega R)\cos\alpha}{(1 + \lambda^2)^{1/2}} \qquad (48)$$

$$\Delta C_{mb} = \frac{-0.568(\dot{\alpha}C/\omega R)\cos\alpha}{(1 + \lambda)^{1/2}} \qquad (49)$$

Equations (48) and (49) must be added to the blade lift and pitching moments presented in Eq (32). The induced drag coefficient can be obtained from the over-all blade lift coefficient (including corrections) as follows:

$$C_{Dib} = C_{Lb}^2/\pi Ae \qquad (50)$$

where e is the Oswald efficiency factor and may be taken as 0.80. This value is added to the sinusoidal base shown in Fig. 4 at the corresponding angle of attack α_0.

Results of the Computer Study

A computer program was developed utilizing the idealized mathematical model presented. Some of the numerical results of interest are discussed in this section.

Region of Stall

The region of stall corresponds to a given angular range in the blade orbit in which the blade stalls in the conventional

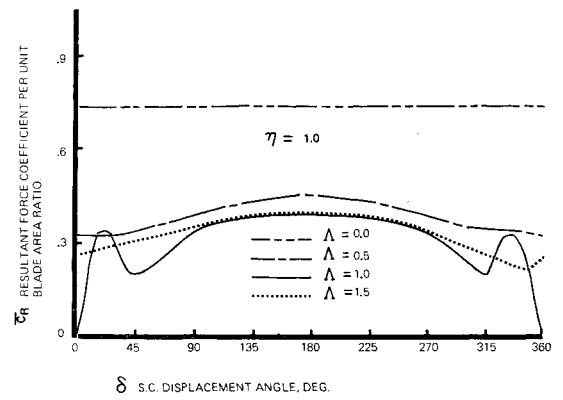

Fig. 10 Resultant force coefficient per unit blace area ratio vs the steering center displacement angle for a pitch ratio of 1.0 and true advance ratios from 0 to 1.5.

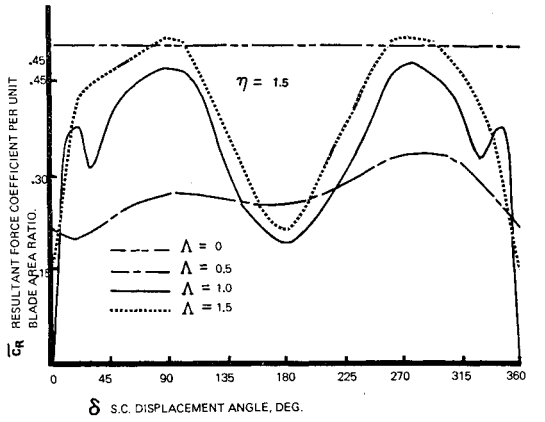

Fig. 11 Resultant force coefficient per unit blade area ratio vs the steering center displacement angle for a pitch ratio of 1.5 and advance ratios from 0 to 1.5.

hydrodynamic sense. As the blade undergoes a complete orbit, it may experience the following possibilities.

1) It never stalls. This condition was found to occur mostly in near-cruise conditions (Λ approaching 1 and δ in the vicinity of 0, which corresponds to a forward thrust mode). This feature is true for the autorotation mode as well. The allowable δ was found to be more restricted for the curtate ($\eta > 1$) propellers than for the prolate ($\eta < 1$) propellers. For $\eta = 1.5$, the allowable range was $-5° < \delta < 5°$ whereas for $\eta = 0.5$, the allowable range was $-20° < \delta < 20°$.

2) It stalls throughout. Complete stall throughout the blade orbit came about under the following situations: a) $\Lambda = 1$, $30° < \delta < 330°$, $\eta = 1$ and b) $\Lambda = 1$, $\eta = 1.5$, and $30° < \delta < 90°$ as well as $270° < \delta < 330°$. The prolate propeller was found to always unstall at some point in its orbit.

3) It stalls and unstalls twice per revolution. This condition was found to be the most predominant case except when $\Lambda = 1$ or $\eta = 1$. The stall-region pair was found not to be symmetrical in θ in either magnitude or direction primarily due to the asymmetric contribution of hysteresis and Kramer's effect. The π-pitched ($\eta = 1$) propeller was found not to be subjected to this condition throughout the range $0 < \delta < 360°$ and $0 < \Lambda < 1.5$.

4) It stalls and unstalls once per revolution. This region bridges the aforementioned condition 1 or condition 2 into condition 3 for the prolate and curtate propellers and spans a range in δ of approximately 15°. The π-pitched ($\eta = 1$) propeller experiences a sudden change from condition 1 to condition 2 at values of Λ approaching 1. Otherwise, it stalls and unstalls only once per revolution for all δ.

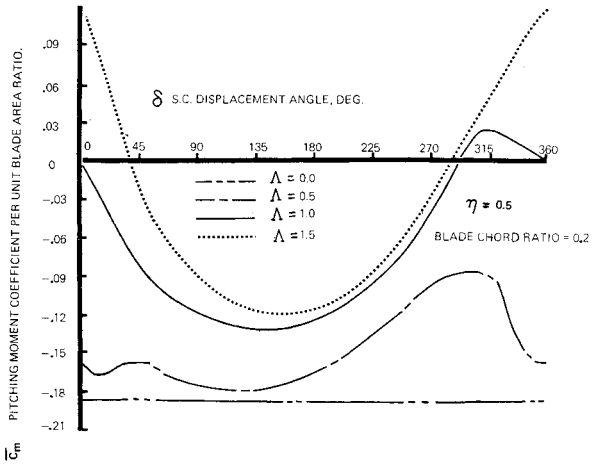

Fig. 12 Pitching moment coefficient per unit blade area ratio vs steering center displacement angle at a pitch ratio of 0.5 for advance ratios from 0 to 1.5.

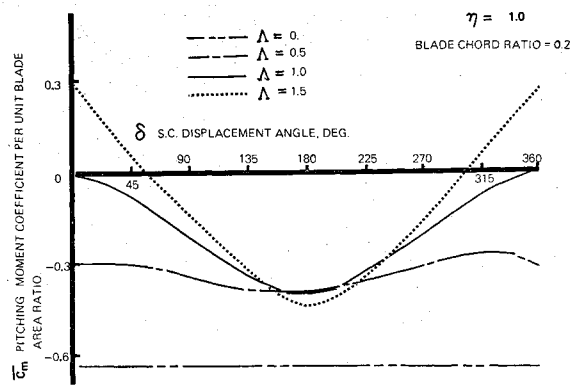

Fig. 13 Pitching moment coefficient per unit blade area ratio vs steering center displacement angle at a pitch ratio of 1.0 for advance ratios from 0 to 1.5.

Kramer's effect and hydrodynamic hysteresis produce very similar consequences both qualitatively and quantitatively. Kramer's effect is associated with the angle of attack rate $\dot{\alpha}$, whereas hydrodynamic hysteresis is associated with the region of stall. These were found to rotate the resultant thrust in a direction opposite to the blade orbit. A slight variation in the magnitude of the resultant thrust vector was present which for all practical purposes may be considered negligible. The combined contribution of Kramer's effect and hydrodynamic hysteresis was found to rotate the resultant thrustline as much as 20° (roughly distributed 10° apiece). At $\Lambda = \eta/\lambda = 1$ and $\delta = 0$, Kramer's effect was conspicuously absent since in this case from Eq. (12), $\alpha_0 = 0$ throughout the orbit and therefore $\dot{\alpha} = 0$.

Resultant Hydrodynamic Forces and Moments

Resultant hydrodynamic forces and moments can be defined by a magnitude and direction. For the choice of direction of the force vector, it is convenient to define a resultant force orbit angle θ_R measured from the drag axis since component vectors would resolve into the resultant lift and drag. For the choice of magnitude, the resultant force coefficient is best presented per unit blade area ratio, by dividing C_R given in Eq. (35) by B

$$\bar{C}_R \equiv C_R/B \tag{51}$$

This coefficient can be directly compared with airfoil data since the reference areas corresponding equally. A similar definition is applicable to the pitching moment coefficient which at $\Lambda < 1$ is the torque coefficient which the motor must overcome in order to maintain a propulsive force

$$\bar{C}_m \equiv C_m/B \tag{52}$$

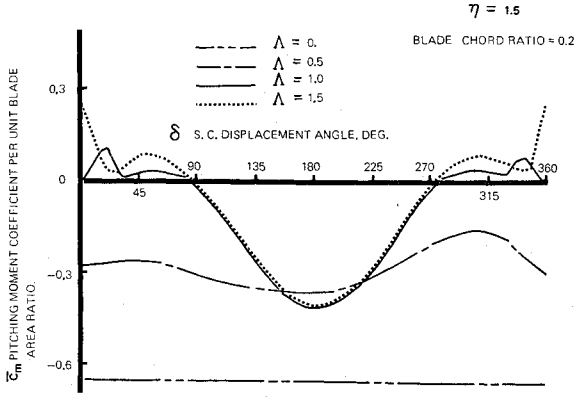

Fig. 14 Pitching moment coefficient per unit blade area ratio vs steering center displacement angle at a pitch ratio of 1.5 for advance ratios from 0 to 1.5.

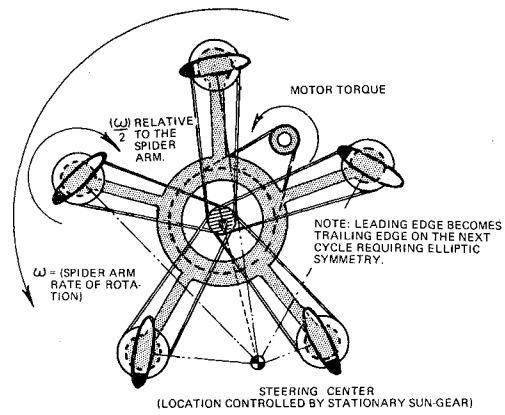

Fig. 15 A wide-sweep belt driven π-pitched cycloidal propeller ($\eta = 1$).

In this case, the chord ratio must be stipulated since the first term in (52) in Eq. (33) is a function of the chord ratio. A chord ratio of 0.2 was employed in the computer study. For small values of chord ratio, the blade area is predominant and the definition given in Eq. (52) may be employed as an approximation valid for the chord ratio range $0 < C/R < 0.25$. The resultant force orbit angle θ_R is plotted against δ for $0 < \Lambda < 1.5$ and $\eta = 0.5$ in Fig. 6. Figures 7 and 8 correspond to a blade pitch ratio of $\eta = 1.0$ and $\eta = 1.5$, respectively. At hover conditions ($\Lambda = 0$), the relationship between θ_R and δ is linear and one-to-one. A 10° counterclockwise rotation in δ results in a 10° counterclockwise rotation of the resultant force vector. At $\delta = 0$, the thrustline is approximately 250° counterclockwise of the steering center. The idealized model used by Seeley[2] not employing either Kramer's effect or hysteresis placed the vector 270° counterclockwise of the steering center. The θ_R vs δ linearity is lost for $\Lambda > 0$. In the forward thrust mode (Λ approaching 1 from below and $-20° < \delta < 20°$), the slope of the θ_R vs δ curve increases. This increase was found to be more pronounced for the curtate propellers. A 10° change in δ (or the sudden surge of a cross current for that matter) now results in a twenty degree (or more) change in θ_R (autostability observed by Kirsten in cross-currents). At $\Lambda \geq 1$, Figs. 6–8 clearly show that for all δ the thrust direction is restricted to $-80° \leq \theta_R \leq 80°$. Under these conditions, a drag component is, therefore, always present and the vehicle cannot possibly be propelled. In fact, for certain δ, the forward velocity of the vehicle can

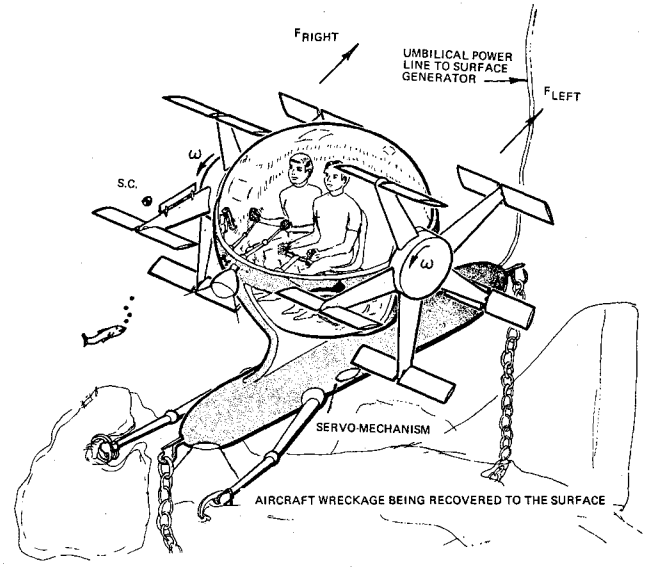

Fig. 16 A sample application of cycloidal propulsion on submersibles.

keep the propeller rotating and lateral forces can be achieved by properly orienting δ. The propeller is then said to be in autorotation. The magnitude of the resultant thrust complementing Figs. 6–8 is correspondingly plotted in Figs. 9–11, thereby defining the thrust vector for all δ, η, and Λ considered here. At $\delta = 0$ and $\Lambda = 1$, the thrust vector vanishes due to the fact that in this case the angle of attack is zero throughout and that a symmetrical airfoil was employed in this study. The highest force coefficient occurs at zero advance ratio, indicating that cycloidal propulsion is well suited for underwater cargo handling operations at near hovering conditions. The propulsion force decreases as Λ approaches 1. The drag of the vehicle would, of course, determine the value of the advance ratio at cruising conditions. Low-drag and high-lift forces can be attained at $|\delta| \approx 45°$ for all η. At apparent advance ratios λ less than 1, the π-pitched ($\eta = 1$) cycloidal propeller was found to provide superior performance, assuming, of course, equal blade designs. The fore and aft symmetry required for $\eta = 1$, however, imposes a fairly severe restriction. At apparent advance ratios greater than 1, the curtate ($\eta > 1$) propellers were found to excel. Figures 12–14 present the pitching moment (torque) coefficients due to cycloidal action. The positive moment coefficient in the low ranges of $|\delta|$ and $\Lambda > 1$ indicates that the propeller in autorotation tends to stabilize at a true advance ratio of unity since the propeller must speed up. For the middle ranges of δ, the pitching moment coefficient is always negative and the propeller would slow down and may even come to a halt. Feathered autorotation is mostly feasible at $-45° < \delta < 45°$. This range is broader for the curtate propellers. In the powered mode ($\Lambda < 1$), the moment coefficient is, in fact, the torque coefficient required for propulsion.

Conclusion

Kramer's effect was found to rotate the resultant propeller thrust by approximately 10°. Cycloidal propellers at cruise conditions were found not to stall and should be fairly quiet. Excellent thrust control is exhibited in the powered and autorotation modes for all advance ratios and pitch ratios. Dynamic stability against cross currents in an inherent characteristic of the propulsive mode and was found more pronounced for the curtate propellers. The π-pitched propeller exhibits the highest efficiency at apparent advance ratios less than unity whereas above unity the curtate propellers excel. Cycloidal propellers approach the efficiency of standard marine screw propellers and exhibit the thrust dexterity of a swivel jet. One such application in submersibles, employing a Kirsten propeller (Fig. 15), is shown in Fig. 16.

References

[1] Kirsten, F. K., "A New Type of Propeller," *Journal of the Society of Automotive Engineers*, Jan. 1928; also *Transactions of the ASME, Cycloidal Propulsion Applied to Aircraft*, Vol. 49–50, Pt. I, AER-FSP, pp. 1927–1928.

[2] Seeley, L. W., "The Stabilizing Potential of the Cycloidal Propeller," TN 4064-6, May 1963, Naval Ordnance Test Station, China Lake, Calif.

[3] Mueller, H. F., "Recent Developments in the Design and Application of the Vertical Axis Propeller," paper presented at the Spring Meeting of the Society of Naval Architects and Marine Engineers in Philadelphia, Pa., May 19, 1955.

[4] Henry, C. J., "A Survey of Cycloidal Propulsion," Rept. 728, Davidson Lab., Stevens Institute of Technology, Dec. 1959, Hoboken, N. J.

[5] Perkins, C. D. and Hage, R. E., *Airplane Performance Stability and Control*, Wiley, New York, 1953.

[6] Hoerner, S. R., *Fluid Dynamic Drag*, book published by the author 1965, Library of Congress Catalog Card Number 64-1966.

[7] Abbott, Doenhoff, A. E., and Stivers, L. J., Jr., "Summary of Airfoil Data," Rept. 824, 1945, NACA.